

Article

Microplotter Printing of Hierarchically Organized NiCo₂O₄ Films for Ethanol Gas Sensing

Tatiana L. Simonenko ^{1,*}, Nikolay P. Simonenko ¹, Artem S. Mokrushin ¹, Philipp Yu. Gorobtsov ¹, Anna A. Lizunova ², Oleg Yu. Grafov ³, Elizaveta P. Simonenko ^{1,*} and Nikolay T. Kuznetsov ¹

¹ Kurnakov Institute of General and Inorganic Chemistry of the Russian Academy of Sciences, 31 Leninsky pr., Moscow 119991, Russia

² Moscow Institute of Physics and Technology, National Research University, 9 Institutskiy per., Dolgoprudny 141701, Russia

³ A. N. Frumkin Institute of Physical Chemistry and Electrochemistry of the Russian Academy of Sciences, 31 Leninsky pr., Moscow 119071, Russia

* Correspondence: egorova.offver@gmail.com (T.L.S.); ep_simonenko@mail.ru (E.P.S.)

Abstract: Using a combination of chemical coprecipitation and hydrothermal treatment of the resulting dispersed system, a hierarchically organized NiCo₂O₄ nanopowder was obtained, consisting of slightly elongated initial oxide nanoparticles self-organized into nanosheets about 10 nm thick, which in turn are combined into hierarchical cellular agglomerates of about 2 μm. Fourier-transform infrared spectroscopy (FTIR), X-ray diffraction analysis (XRD), selected area electron diffraction (SAED) and high-resolution transmission electron microscopy (HR-TEM) allowed to confirm the formation of NiCo₂O₄ powder with the desired crystal structure via additional heat treatment of the intermediate product. Energy-dispersive X-ray spectroscopy (EDX) was used to confirm the target metal ratio, and the uniform distribution of the elements (Ni, Co and O) was shown by mapping. The resulting nanopowder was employed to prepare functional inks suitable for microplotter printing of the NiCo₂O₄ film. It was found that an oxide film morphology is fully inherited from the hierarchically organized oxide nanopowder used. Atomic force microscopy (AFM) revealed the film thickness (15 μm) and determined the maximum height difference of 500 nm over an area of 25 μm². Kelvin probe force microscopy (KPFM) showed that the surface potential was shifted to the depths of the oxide film, and the work function value of the material surface was 4.54 eV, which is significantly lower compared to those reported in the literature. The electronic state of the elements in the NiCo₂O₄ film under study was analyzed by X-ray photoelectron spectroscopy (XPS). Chemosensor measurements showed that the printed receptor layer exhibited selectivity and high signal reproducibility for ethanol detection. As the relative humidity increases from 0 to 75%, the response value is reduced; however, the sensor response profile and signal-to-noise ratio remain without significant changes.



Citation: Simonenko, T.L.; Simonenko, N.P.; Mokrushin, A.S.; Gorobtsov, P.Y.; Lizunova, A.A.; Grafov, O.Y.; Simonenko, E.P.; Kuznetsov, N.T. Microplotter Printing of Hierarchically Organized NiCo₂O₄ Films for Ethanol Gas Sensing. *Chemosensors* **2023**, *11*, 138. <https://doi.org/10.3390/chemosensors11020138>

Academic Editor: Dongzhi Zhang

Received: 6 January 2023

Revised: 4 February 2023

Accepted: 9 February 2023

Published: 14 February 2023

Keywords: programmable coprecipitation; hydrothermal synthesis; NiCo₂O₄; nanopowder; film; spinel; microplotter printing; electrode; gas sensor; supercapacitor



Copyright: © 2023 by the authors. Licensee MDPI, Basel, Switzerland. This article is an open access article distributed under the terms and conditions of the Creative Commons Attribution (CC BY) license (<https://creativecommons.org/licenses/by/4.0/>).

1. Introduction

Transition metal oxides (TMOs), especially metal cobaltites (MCo₂O₄, M = Cu, Zn, Mn, Ni) with spinel structure, owing to their catalytic and electrochemical characteristics are nowadays very promising materials in such practically important fields as alternative energy [1–3], catalysis [4,5], optics [6,7], gas [8,9] and biosensors [10,11]. It is also noted that such complex composition oxides exhibit improved functional characteristics compared to the individual metal oxides comprising them. Thus, NiCo₂O₄ is an inverse spinel, a typical *p*-type semiconductor combining two metal cations capable of forming two redox couples: Ni³⁺/Ni²⁺ (0.58 V/0.49 V) and Co³⁺/Co²⁺ (0.53 V/0.51 V) [10]. Such reversible processes can provide donor-acceptor sites for chemisorption of gas molecules and promote

their subsequent reversible adsorption [10,12]. Thus, the high redox activity and electrical conductivity (at least two orders of magnitude higher than those of individual cobalt and nickel oxides [13]), as well as the commercial availability of nickel-cobalt spinel make it a very attractive receptor material for resistive gas sensors. For instance, a number of works report on the development of sensor systems based on NiCo_2O_4 sensitive to H_2 [14], NO_2 [12], as well as to a number of volatile organic compounds (acetone [15], xylene [16], n-butanol [17] and ethanol [18]). In the case of ethanol, the pure NiCo_2O_4 used by the authors was characterized by a rather low sensory response, which may be due to an insufficiently developed surface of the material. Its modification with tin dioxide particles enhanced the chemosensory properties, but led to a complication of the synthesis method.

Other metal oxide-based materials are applied as receptor components used for ethanol gas sensing. In particular, metal oxide semiconductor heterojunctions (MOSHs) [19,20], which are characterized by low operating temperatures and improved kinetic parameters, have recently received much attention in this context. A common chemosensor material such as zinc oxide is also very effective for the detection of ethanol vapor in the ambient atmosphere. In this case the functional properties can be improved by modifying it with noble metals or rare-earth element oxides [21]. Using methods that allow the formation of anisotropic oxide structures, the chemosensory properties of the materials in ethanol detection can be further improved [22].

To improve the performance characteristics (magnitude and time of sensory response, selectivity) of the receptor materials, researchers tend to form nanomaterials with hierarchically organized microstructure (including those consisting of anisotropic particles), which, as a rule, leads to surface development and significant functional properties enhancement. In particular, a number of papers have shown that such an approach makes it possible to reduce charge (ion/electron) transfer distance and enlarge the active surface area of the obtained materials. In turn, this contributes to increased number of surface active centers and selectivity, as well as improved kinetic characteristics of the receptor materials [17,23]. Additionally, the features of the material's pore structure have a significant impact on its other functional characteristics [24].

Among the strategies for hierarchical nanostructures formation are coprecipitation, microemulsion synthesis, sol-gel technology, electrospinning, as well as hydrothermal and solvothermal methods [25–27]. In the present study, in order to ensure the primary nucleation under controlled conditions, we used a programmable chemical coprecipitation of intermediates, which enables fine control of the reagent mixing kinetics, taking into account the pH value of the reaction system that changes as a result of their interaction. The hydrothermal treatment of the obtained disperse system was further performed to initiate additional self-organization of initial nanoparticles. According to the literature data, the hydrothermal method enables the formation of the most diverse spectrum of morphologies: hollow spheres [28–30], nanotubes, nanofibers, nanorods and nanoneedles [31–34], nanosheets and lamellar structures [35–37] or nanoflowers [38–40].

The microstructure and functional characteristics of the receptor layers formed are greatly determined not only by the active material synthesis method, but also by the film deposition method as well. The continuous trend toward miniaturization of microelectronic devices in general and resistive gas sensors in particular, as well as the need to create their components in the form of complex geometry planar nanostructures, requires the use of modern high-technology deposition methods. In this context, additive technologies (inkjet printing [41–44], aerosol jet printing [45–47], pen plotter printing [48–50], microplotter printing [51–53] and microextrusion printing [54–58]), which enable automated reproducible application of coatings of different thicknesses and geometries to various, have recently become increasingly popular.

The aim of this work was to study the synthesis process of hierarchically organized nickel-cobalt spinel using programmed chemical coprecipitation followed by hydrothermal treatment of the resulting disperse system, to develop a microplotter printing technique of

the corresponding film on the chip surface and to examine chemosensory properties of the obtained material.

2. Materials and Methods

2.1. Materials

$\text{NiCl}_2 \cdot 6\text{H}_2\text{O}$ (>98%, Lenreactiv, St. Petersburg, Russia), $\text{Co}(\text{NO}_3)_2 \cdot 6\text{H}_2\text{O}$ (>98%, Lenreactiv, St. Petersburg, Russia), triethanolamine ($\text{C}_6\text{H}_{15}\text{NO}_3$, 99%, Chimmed, Moscow, Russia) of analytical grade were used in this work without a further purification.

2.2. Preparation of NiCo_2O_4 Nanopowder

NiCo_2O_4 nanopowder was obtained by combining the programmed chemical coprecipitation method with hydrothermal treatment of the resulting solid phase particles. Chemical coprecipitation was carried out using an ATP-02 automatic high-precision potentiometric titrator equipped with a built-in pH meter (Aquilon JSC, Podolsk, Russia). At the first stage, a 10% aqueous solution of triethanolamine was automatically added (supply pulse was 3 s with a pause between pulses being 2 s) to 10 mL aqueous solution of inorganic metal salts (total metal concentration was 0.1 mol/L) heated to 60 °C until reaching pH 9.7 to achieve full conversion of metal-containing reagents. The resulting disperse system was transferred into a 25 mL Teflon-lined stainless-steel autoclave and subjected to hydrothermal treatment at 140 °C for 2 h. After the system cooled naturally to 25 °C, the dispersed phase was separated and washed with distilled water by cyclic centrifugation followed by drying of the intermediate at 100 °C for 5 h. Then, considering the thermal analysis results, additional heat treatment (400 °C, 5 h) of the obtained powder was carried out in ambient atmosphere to crystallize the target NiCo_2O_4 oxide with spinel structure.

2.3. Microplotter Printing of Hierarchically Organized NiCo_2O_4 Film

The obtained anisotropic NiCo_2O_4 nanopowder was further used to prepare a stable disperse system (10 wt% oxide particle content) in α -terpineol in the presence of a binder (ethylcellulose), appropriate as functional inks for microplotter printing of an oxide film on the surface of a specialized Pt/ Al_2O_3 /Pt chip ($R_a = 100$ nm, geometric dimensions $4.1 \times 25.5 \times 0.6$ mm). A capillary with a channel diameter of 150 μm was used as a dispenser. The automated application of an ink layer with lateral dimensions of 5×3 mm on the chip surface in the area of preliminary applied platinum interdigitated electrodes was carried out using a three-coordinate positioning system after the dispersion system meniscus contacted the substrate surface in accordance with the digital pathway. After touching the chip surface, the dispenser was moved in the lateral plane along a zigzag trajectory with a distance between the lines of 100 μm . Due to wetting of the substrate, the ink was spontaneously extracted from the capillary without additional external activation. Once the printing program was completed, the dispenser was automatically moved along the vertical axis by 1 mm above the film and moved away from the sample. The formed ink film was further subjected to a stepwise drying in the temperature range of 25–50 °C (5 h) for solvent evaporation, followed by an additional heat treatment at 350 °C (1 h) for binder removal. The preparation steps of NiCo_2O_4 powder and a corresponding film microplotter printing are presented in Figure 1.

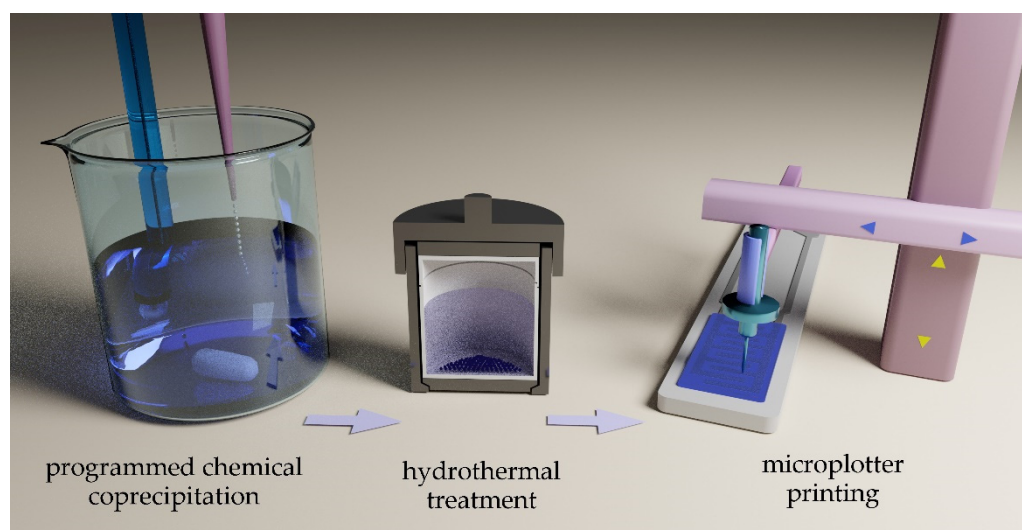


Figure 1. Schematic illustration of hierarchically organized oxide synthesis and microplotter printing of the corresponding film on a chip.

2.4. Instrumentation

Thermal stability of the as-synthesized product was examined by synchronous (TGA/DSC) thermal analysis (SDT Q-600 thermal analyzer, TA Instruments, New Castle, DE, USA) in an air flow (250 mL/min) in the temperature range of 25–1000 °C (controlled heating was performed in Al₂O₃-microcrucibles at a speed of 10°/min, powder mass was 1.414 mg).

IR transmission spectra of powders were recorded in the wavelength range of 350–4000 cm⁻¹ (signal accumulation time 15 s and resolution 1 cm⁻¹; InfraLUM FT-08 FT-IR spectrometer, Lumex, St. Petersburg, Russia). For this purpose, suspensions using powders after synthesis and also after additional heat treatment were prepared in Vaseline oil and then placed between KBr glasses in the form of films.

XRD patterns of the powders under study were obtained on a Bruker D8 Advance diffractometer (Bruker, Bremen, Germany; CuK α = 1.5418 Å, Ni-filter, E = 40 keV, I = 40 mA, 2 θ range—5°–80°, resolution—0.02°, signal accumulation time was 0.3 s and 2.0 s; for the coating analysis at 2 θ range—28°–45°).

The microstructure of the resulting NiCo₂O₄ nanopowder and the corresponding film formed on its basis were studied by SEM (Carl Zeiss NVision-40, Carl Zeiss, Inc., Oberkochen, Germany). TEM was also used for microstructure analysis, selected area electron diffraction and elemental mapping on the surface of oxide agglomerates (JEOL JEM-1011 equipped with ORIUS SC1000W digital camera; JEOL JEM2100 with X-MaxN Oxford Instruments EDX spectrometer; JEOL Ltd., Akishima, Japan).

The printed coating was also investigated by AFM and KPFM methods (NT-MDT Solver PRO microscope (NT-MDT, Zelenograd, Russia); ETALON HA_HR probes (ScanSens, Bremen, Germany) with W₂C conductive coating (rounding radius < 35 nm). The work function of the material surface (ϕ_{film}) was calculated in the course of the KPFM measurement. First, the film surface was scanned using a probe with a preknown work function value (ϕ_{tip}), the mean contact potential (ϕ_{CPD}) value was measured and then ϕ_{film} was determined as the difference between ϕ_{tip} and ϕ_{CPD} .

X-ray photoelectron spectroscopy (XPS) studies were performed using an OMICRON ESCA + spectrometer (Scienta Omicron, Taunusstein, Germany) with an aluminum anode equipped with an AlK α XM1000 monochromatic X-ray source (with an emission energy of 1486.6 eV and a power of 252 W). A CN-10 charge neutralizer with an emission current of 4 μ A and a beam energy of 1 eV was used to eliminate the local charge on the analyzed surface. The transmittance energy of the analyzer was 20 eV. The spectrometer was calibrated using the Au4f 7/2 line at 84.1 eV. The pressure in the analyzer chamber did not

exceed 10^{-9} mbar. All spectra were accumulated at least eight times. Fluctuation of the peak positions did not exceed ± 0.1 eV.

Chemosensory tests were conducted on a precise laboratory setup. Two Bronkhorst gas flow controllers (Bronkhorst Instruments GmbH, Leonhardsbuch, Germany) with a maximum throughput of 100 and 200 mL/min were employed to create a gas environment in the quartz cell with a volume of 7×10^{-5} m³. A Fluke 8846A Digit Precision Multimeter with an upper detection limit of 1000 M Ω (Fluke Corporation, Everett, Washington, DC, USA) was used to control electrical resistance of the film printed on the specialized Pt/Al₂O₃/Pt chip, and its temperature was monitored with a platinum micro-heater pre-calibrated with a high-precision Testo 868 thermal imager (Testo, Lenzkirch, Germany). Hydrogen (H₂), carbon monoxide (CO), ammonia (NH₃), benzene (C₆H₆), ethanol (C₂H₅OH) and acetone (C₃H₆O) responses were measured using the corresponding calibration gas mixtures with air. To measure the sensory signal at different relative humidity (RH) level, a special unit with a bubble flask was utilized and the gas mixture RH was controlled by an Eksis digital flow-through hygrometer (Eksis, Zelenograd, Russia). The temperature value of the relative humidity was set and then measured at 20 °C.

3. Results and Discussion

3.1. Characterization of the Intermediate Product and the Obtained NiCo₂O₄ Nanopowder

The thermal behavior of the obtained intermediate product was studied by a synchronous (TGA/DSC) thermal analysis in air (Figure 2). The corresponding TGA curve shows that in the temperature range under study the powder undergoes 3 main steps of mass loss: in the interval of 25–250 ($\Delta m = 15\%$), 250–300 (28%) and 300–900 °C (8%). Including some mass loss during the final heating stage, the total Δm value was 51.6%. However, a thermal effect (with a maximum at 264 °C) characterized by significant energy release was observed only for the second step of mass change. This exo-effect, presumably, is connected with crystallization of the target oxide (NiCo₂O₄). Such thermal behavior of the intermediate product, according to the literature data [59], may indicate the presence of nickel-cobalt hydroxocarbonate in its composition. The first stage of the mass loss can be related to the residual solvent evaporation and the intermediate product partial decomposition. During the third stage of mass loss the semiproduct decomposition is probably continued, passing about 850 °C to the formed NiCo₂O₄ degradation, accompanied by the oxygen release. Thus, in order to fully decompose the semiproduct and prevent the target material degradation a sufficiently long additional heat treatment of the sample at relatively low temperatures is required. Given the thermal analysis results the following mode of the intermediate product additional heat treatment has been chosen: 400 °C, 5 h.

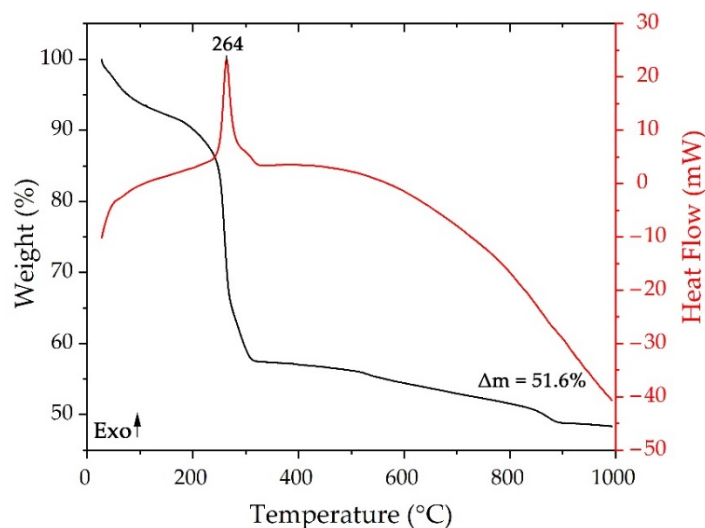


Figure 2. Results of synchronous (TGA/DSC) thermal analysis of the semiproduct.

The set of functional groups in the semiproduct and the resulting NiCo_2O_4 nanopowder was determined by FTIR spectroscopy (Figure 3). The spectrum of the intermediate product exhibits a broad absorption band at $3100\text{--}3700\text{ cm}^{-1}$ and another absorption band with a maximum at about 1646 cm^{-1} related to the $\nu(\text{O-H})$ and $\delta(\text{O-H})$ vibrations, respectively, which are characteristic of the nickel-cobalt layered double hydroxide (LDH) [60,61]. At the same time, the powder spectrum shows an absorption band with a maximum of about 1584 cm^{-1} and a complex band in the range of $990\text{--}1190\text{ cm}^{-1}$, which may be related to $\nu(\text{CO}_3^{2-})$ and $\nu(\text{CO}_3^{2-})$ carboxylate groups vibrations [62,63], indicating the presence of metal hydroxocarbonate in the material composition. Two absorption bands with maximums at 647 and 555 cm^{-1} related to vibrations of (Co-O) and (Ni-O) groups, respectively, and characteristic for the NiCo_2O_4 oxide with spinel structure were observed in the spectrum of the powder obtained by additional thermal treatment at $400\text{ }^\circ\text{C}$ [64]. No functional groups from any impurities (reagents or by-products) were detected in the powders.

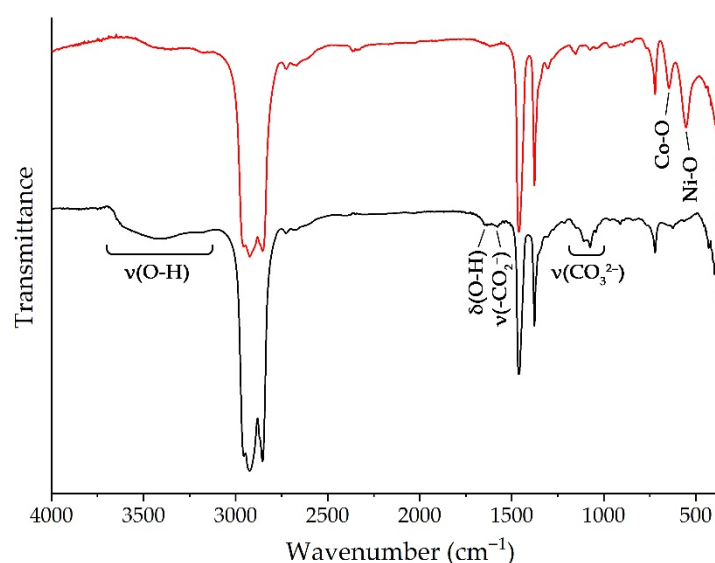


Figure 3. FTIR spectra of the semiproduct (black) and the obtained NiCo_2O_4 nanopowder (red).

The crystal structure of the intermediate product and its transformation as a result of additional heat treatment when obtaining the target NiCo_2O_4 oxide was studied with X-ray diffraction analysis (Figure 4). Thus, in the case of the intermediate product, the main set of reflections at 2θ value of 8.3° (significantly shifted to the small-angle region), 24.9° , 33.2° and 59.2° can be indexed to the (003), (006), (101) and (110) planes of hydrotalcite-like NiCo LDH phase [60]. The reflection at 16.7° (marked with a *), which is not related to this phase, was also observed in [65], where triethanolamine was used as one of the reaction system components. The authors of this work did not attribute this signal to any compound. We attribute the existence of the corresponding reflection to the formation of hexagonal metal carbonate hydroxide hydrate of the composition $\text{M}(\text{CO}_3)_{0.5}\text{OH}\cdot 0.11\text{H}_2\text{O}$ (where M is nickel and cobalt cations) being one of the semiproduct components [66]. The average size of the coherent scattering region (CSR) of the main semiproduct component was $13.2 \pm 1.5\text{ nm}$, and for the carbonate hydroxide hydrate this parameter has a value of $8.9 \pm 1.0\text{ nm}$. The XRD results for the semiproduct agree well with the data of its thermal analysis, as well as with the FTIR results. The set of reflections on the XRD pattern of the oxide powder corresponds well to the target NiCo_2O_4 crystal structure (space group Fd3m, PDF # 73-1702) [64]. No reflections from the intermediates or decomposition products of the target material are observed in this case, which testifies to the optimal heat treatment mode of the powder. The average CSR size for the obtained NiCo_2O_4 oxide is $9.0 \pm 1.0\text{ nm}$, i.e., the material has a nanocrystalline state.

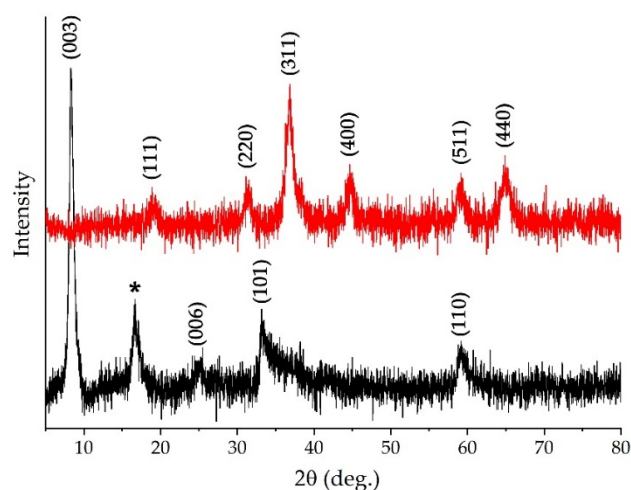


Figure 4. XRD patterns of the intermediate product (black) and the resulting NiCo_2O_4 nanopowder (red). The “*” marker indicates a reflex referring to $\text{M}(\text{CO}_3)_{0.5}\text{OH}\cdot 0.11\text{H}_2\text{O}$ (where M is nickel and cobalt cations).

The microstructure of the obtained NiCo_2O_4 nanopowder was studied by scanning electron microscopy (Figure 5a,b). As can be seen from the micrographs, the material has several levels of organization. Thus, initial spherical nanoparticles of 10.0 ± 1.0 nm are self-organized into nanosheets of the same thickness, which in turn are combined into hierarchically organized cellular agglomerates about $2 \mu\text{m}$ in size. As a result, the microstructure features of the obtained oxide nanopowder provide access to the ambient atmosphere for almost every primary nanoparticle, which is especially important for achieving a high sorption capacity of the receptor components used in resistive gas sensors.

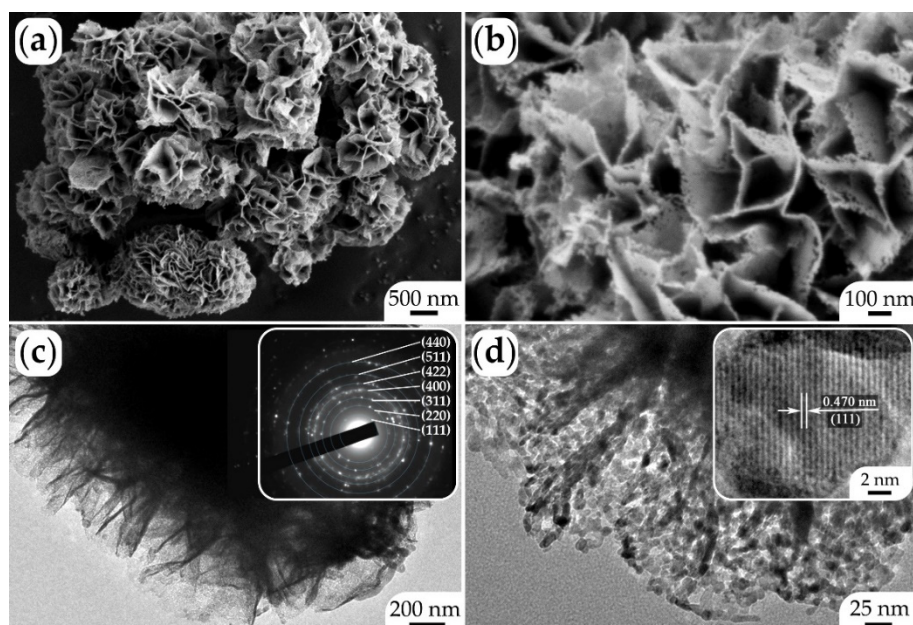


Figure 5. Microstructure (a,b—SEM; c,d—TEM) of the obtained hierarchically organized NiCo_2O_4 nanopowder; SAED (c, inset) and HR-TEM results (d, inset).

Transmission electron microscopy, including high resolution one, was used to further analyze the oxide nanopowder microstructure (Figure 5c,d). The results showed that the initial oxide particles have a slightly elongated shape with an average length of 11.2 ± 1.5 nm and an average thickness of 5.4 ± 0.4 nm. The SAED pattern (Figure 4c, inset) indicates

that the resulting NiCo_2O_4 powder comprises highly crystalline nanoparticles. The diffraction rings correspond to the (111), (200), (311), (400), (422), (511) and (440) planes of the cubic phase (Fd3m), respectively. The HR-TEM image acquired from a single NiCo_2O_4 nanoparticle (Figure 4d, inset) shows lattice fringes matching the crystallographic plane (111) with an average interplanar distance of 0.470 nm.

When studying the microstructure of the oxide powder by the TEM method, the target metal ratio was also confirmed using EDX. In addition, the element distribution maps (Ni, Co and O) on the surface of the oxide particles were built (Figure 6). According to the obtained results, the corresponding elements were evenly distributed on the particle surface of the powder under study. No impurities differing from the basic material in chemical composition or microstructure were revealed.

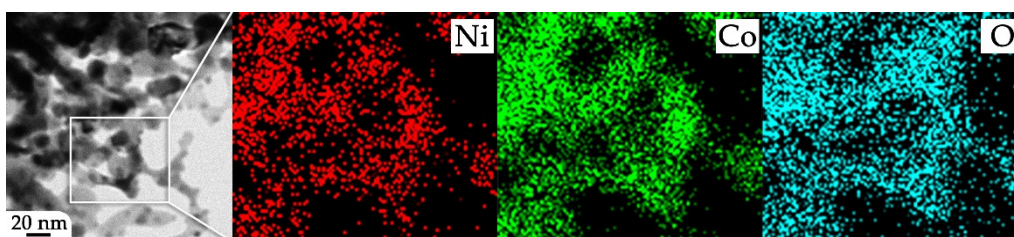


Figure 6. Maps of the element distribution on the surface of the oxide particles (according to TEM and EDX data).

Hence, a hierarchically organized NiCo_2O_4 nanopowder with a spinel structure was obtained by combining the programmed chemical coprecipitation and hydrothermal treatment of the resulting disperse system. The synthesized oxide nanopowder was further used in the preparation of functional inks suitable in their sedimentation stability and rheological characteristics for microplotter printing of the corresponding oxide film as a receptor component of a resistive gas sensor.

3.2. Characterization of Printed NiCo_2O_4 Film

The crystal structure of the NiCo_2O_4 film formed on the Pt/ Al_2O_3 /Pt chip surface was studied by X-ray diffraction analysis (Figure 7). The overview XRD pattern demonstrates (Figure 7, left) the signals from the substrate components (Pt and Al_2O_3) prevail. The most intense (311) reflection related to the oxide film were only detected with a significant increase in the signal accumulation time (Figure 6, right), which can be attributed to the highly dispersed state of the material and its microstructure peculiarities. Therefore, it was shown that the material crystal structure did not undergo any changes during functional ink preparation and oxide film printing, as well as no crystalline impurities appeared.

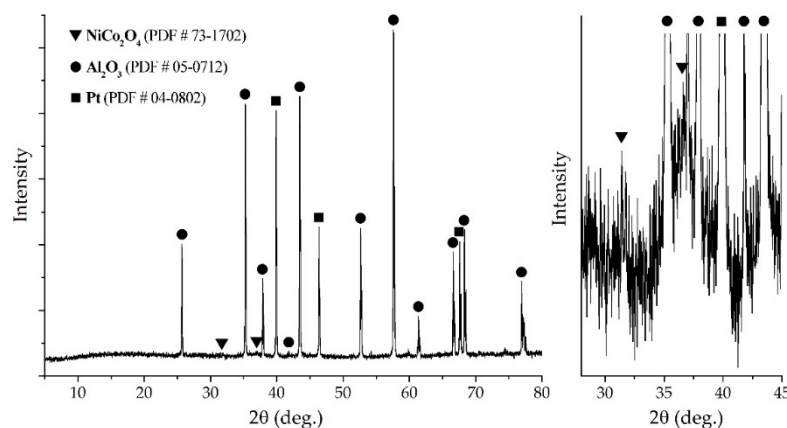


Figure 7. XRD patterns of hierarchically organized NiCo_2O_4 films printed on the Pt/ Al_2O_3 /Pt chip surface (left: 5° – 80° , signal accumulation time of 0.3 s; right: 28° – 45° , 2.0 s).

The microstructure of the printed NiCo_2O_4 film was examined by scanning electron microscopy (Figure 8). It was found that the character of the material morphology was completely inherited from the employed hierarchically organized oxide nanopowder characterized by two levels of particle self-organization. Thus, additional experimental steps involving the formation of a stable disperse system based on oxide particles, film application by microplotter printing and additional heat treatment for solvent and binder removal do not lead to noticeable distortions in the material microstructural features, given by the synthesis conditions. Furthermore, it is shown that the obtained film is highly porous and has a cellular microstructure that provides high sorption capacity and provides access of all NiCo_2O_4 initial nanoparticles to the surrounding atmosphere, which is necessary to ensure high efficiency of the material as a receptor component as part of a resistive gas sensor. Thus, a more detailed analysis of the film pore structure revealed that the pores of the material, as well as the particles, have a multimodal size distribution. In particular, nanosheets are characterized by pores with an average size of 8 ± 2 nm, pores between nanosheets in cellular agglomerates have a size of 200 ± 50 nm and pores between these agglomerates vary in a range of 0.5–2.5 μm . Thus, the obtained film has a complex organization of the pore structure.

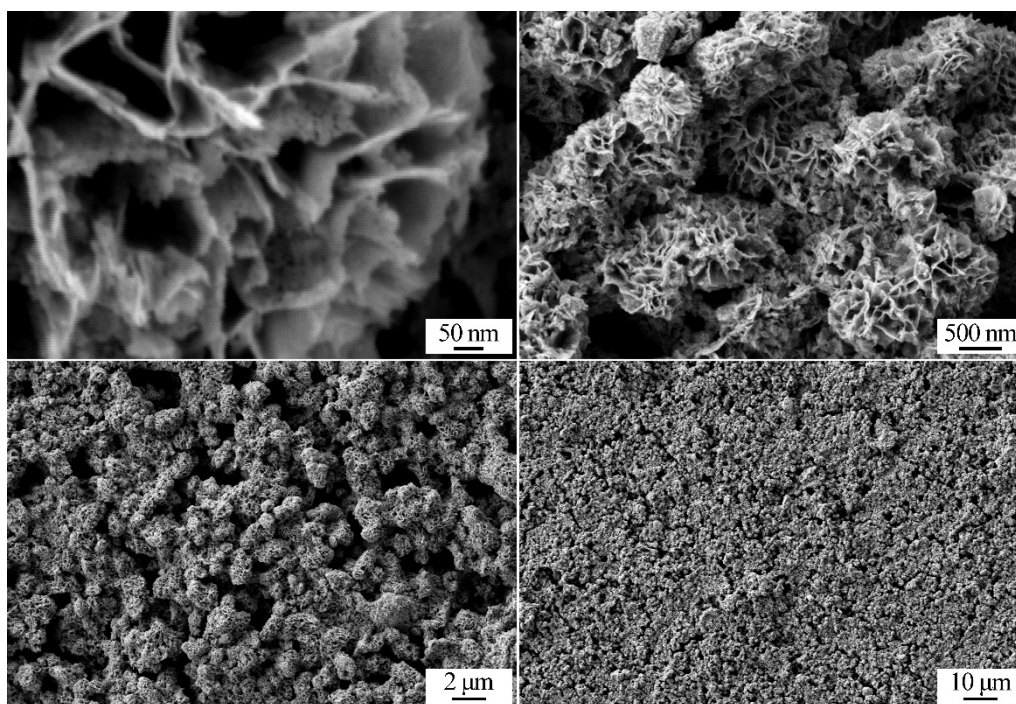


Figure 8. Microstructure of the printed NiCo_2O_4 film (SEM data).

Atomic force microscopy was used to further study the surface morphology of the obtained NiCo_2O_4 film. The topographic image (Figure 9a) shows agglomerates consistent in shape and size with the SEM results. At the same time, the complex structure of these formations composed of self-organized nanosheets of complex shape does not appear in the obtained image, which is related to the peculiarities of the probe used for scanning. The root mean square roughness R_q of the film over an area of $25 \mu\text{m}^2$ was 72 nm, and the maximum height difference in the studied representative area has a value of 500 nm, which confirms the developed surface of the material. At this stage, the thickness of the printed coating (15 μm) was determined.

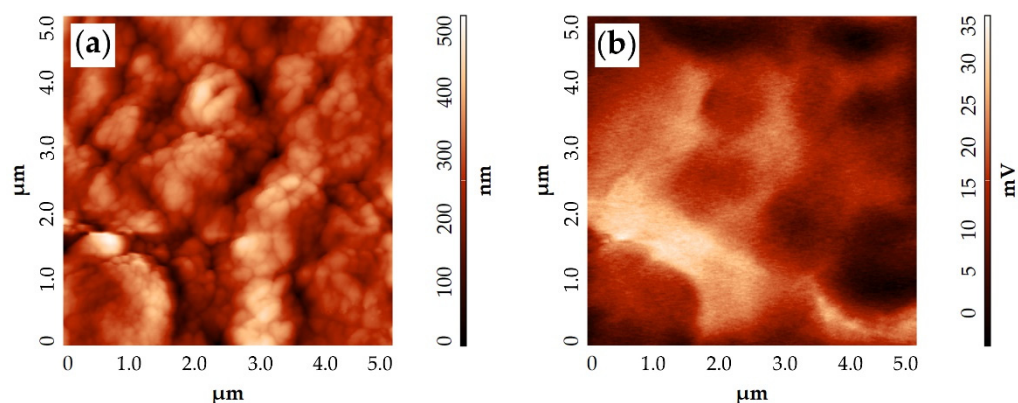


Figure 9. Microstructure of the NiCo_2O_4 film: (a)—topography (AFM), (b)—surface potential distribution map (KPFM).

When studying the NiCo_2O_4 film surface using Kelvin probe force microscopy, the local electrophysical properties of the material were investigated. Thus, the corresponding map (Figure 9b) shows that the surface potential is slightly shifted to depths, which indicates that the charge carriers are shifted to these areas. At the same time, it should be noted that the difference in potential values over a rather large ($25 \mu\text{m}^2$) area with height differences up to 500 nm was only about 35 mV. This indicates a very uniform surface potential distribution and indirectly points to a relatively high conductivity of the film. This result further suggests the high reliability of the electronic work function value of the material surface, established basing on the KPFM data, which was 4.54 eV, considerably lower than that found in the literature (about 5.5 eV) and obtained by analogous methods (Kelvin probe mapping, KPFM) [67,68]. This fact is of particular interest and can point to the specific features of the obtained material associated with an increased oxygen vacancy concentration. For example, a study [69] shows that the NiCo_2O_4 work function decreases when the oxygen vacancy level in the material composition increases. Probably, in our case, these electrophysical properties of the material resulted from the specifics of the synthesis process with the use of triethanolamine as one of the reagents, as well as including the stage of hydrothermal treatment of the solid phase particles formed by the programmed coprecipitation method. A lower work function value for the individual NiO was observed in a previous study [70] where triethanolamine was also applied as a base, but the semiproduct particles were formed directly in hydrothermal conditions.

The electronic state of the elements in the NiCo_2O_4 film was analyzed by XPS (Figure 10). According to the data obtained, the experimental curves of cobalt Co2p and nickel Ni2p are similar to the results of Ref [71]. At the first stage, the spectra of nickel and cobalt were fitted without determining the elements states (Figure 10a,b). The background was subtracted by the Shirley method [72] with the spin-orbit coupling area ratio $2p_{3/2}-2p_{1/2}$ preserved as 2:1. The positions, full width at half maximum (FWHM) values, and the ratios of the peaks to each other were determined (Table 1).

Determination of the element electronic states in the spectra was carried out taking into account the characteristic forms of the spectra for compounds with known stoichiometry, such as NiO, Ni_2O_3 , Co_3O_4 (spectrum form similar to Co_2O_3) and CoO. The spectral shapes of the listed states are complex and include several peaks (Figure 10c,d). According to the obtained results, the two elements are both in the Me^{2+} state and in the Me^{3+} form. In contrast to Ref. [73], the maxima of the cobalt states are shifted to the region of higher values by 0.2 eV, and the maximum of NiO is located at 854.4 eV. The analysis of the obtained data made it possible to determine the peak parameters of the corresponding element states (Table 2).

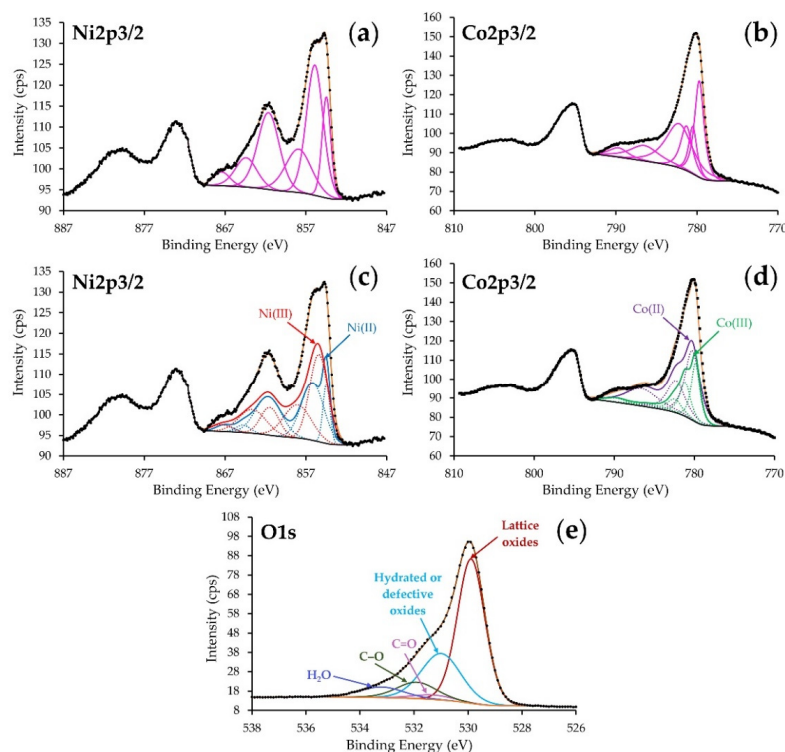


Figure 10. Fitting examples of Ni2p_{3/2} (a) and Co2p_{3/2} (b) spectra of the NiCo₂O₄ film, including the electronic state of the elements (c,d), as well as the results of the O1s spectrum (e) analysis.

Table 1. Fitting parameters of the Ni2p_{3/2} and Co2p_{3/2} spectra without determining the electronic states of the elements: binding energy (eV), percentage of total area, FWHM (eV).

Compound	Ni2p _{3/2}	Co2p _{3/2}
Peak 1 (eV)	854.4	779.7
%	13.16	25.17
FWHM (eV)	1.32	1.40
Peak 2 (eV)	855.9	780.5
%	32.71	10.53
FWHM (eV)	2.57	1.19
Peak 3 (eV)	857.9	781.3
%	16.78	14.39
FWHM (eV)	3.95	1.74
Peak 4 (eV)	861.6	782.2
%	24.59	32.46
FWHM (eV)	3.27	3.97
Peak 5 (eV)	867.41	786.48
%	3.35	12.56
FWHM (eV)	2.47	4.39
Peak 6 (eV)	864.39	789.7
%	9.42	4.89
FWHM (eV)	3.28	2.81

Table 2. Coupling parameters of the Ni2p3/2 and Co2p3/2 spectra with determination of the states: binding energy (eV), percentage of the total area, FWHM (eV).

Compound	Ni2p3/2		Co2p3/2	
	Ni(II)	Ni(III)	Co(II)	Co(III)
Peak 1 (eV)	854.4	855.4	780.2	779.8
%	14.3	42.3	46.6	40.5
FWHM (eV)	1.02	2.67	2.24	1.3
Peak 2 (eV)	856.1	858.0	782.3	781.1
%	44.2	23.8	25.7	29.1
FWHM (eV)	3.25	4.00	2.66	1.62
Peak 3 (eV)	861.6	861.5	785.7	782.4
%	34.0	13.3	1.6	15.2
FWHM (eV)	3.76	2.67	2.29	2.18
Peak 4 (eV)	864.7	867.4	786.6	785.4
%	3.6	3.5	26.1	8.1
FWHM (eV)	2.04	2.91	4.98	4.44
Peak 5 (eV)	867.0	863.6		789.7
%	3.9	17.1		7.1
FWHM (eV)	2.44	4.00		3.29

The O1s oxygen spectrum (Figure 10e), in turn, can be divided into five peaks, two of which relate to oxygen-containing carbon derivatives and are labeled C–O (531.3 eV, FWHM 1.8 eV) and C=O (531.9 eV, FWHM 1.8 eV), a peak at 533.2 eV and FWHM 1.8 eV can be attributed to adsorbed H₂O vapor, and two peaks related to the oxide film material. The maximum of the lattice oxide peak is located at 529.9 eV and has a FWHM of 1.25 eV, while the second peak with a position of 531.0 eV (FWHM 1.8 eV) can be related either to hydrated oxygen atoms on the surface or to oxygen atoms having more positive electronic density than the lattice oxygen. As a result, the concentrations and positions of the maxima for the studied elements were determined (Table 3). Sensitivity factors were determined for substances with known stoichiometry.

Table 3. Concentrations and positions of the elements.

Compound	Ni2p3/2		Co2p3/2		O1s				
	Ni(II)	Ni(III)	Co(II)	Co(III)	L.Ox	H.Ox	C=O	C–O	H ₂ O
Position, eV	854, 4	855, 4	780, 2	779, 8	529, 9	531, 0	531, 3	531, 9	533, 2
Conc., at.%	5, 7	7, 4	16, 0	9, 1	34, 4	16, 1	1, 6	5, 7	4, 0

3.3. Chemosensory Measurements

The sensory response was calculated according to the formula:

$$S = |R_g - R_{Air}| / R_{Air} \quad (1)$$

where R_g is the resistance at a given concentration of the analyte gas; R_{Air} is the resistance in air.

The results of a chemosensor characteristics studies of the printed hierarchically organized NiCo₂O₄ film were used to plot the selectivity diagram containing the sensory response values for the analytes under study in the operating temperature range of 50–300 °C (Figure 11a). The highest sensory response values can be seen for ethanol and acetone in

the 150–300 °C range. At 275–300 °C the material shows almost the same signal for acetone and ethanol, for which the response is, respectively, 54 (300 °C) and 123% (275 °C), and at 225 °C there is a noticeable selectivity to ethanol ($S_{\text{et}} = 84\%$ vs. $S_{\text{ac}} = 48\%$). A further decrease in the operating temperature leads to a significant drop in the ethanol sensory response (down to 40–54%, 150–200 °C). Signals to other analytes in the entire temperature range do not exceed 39% (CO, 150 °C). The response value for other gases (except ethanol and acetone) at 225 °C does not exceed 28%. Further, the chemosensory properties of the oxide film were studied when detecting ethanol at 225 °C in more detail.

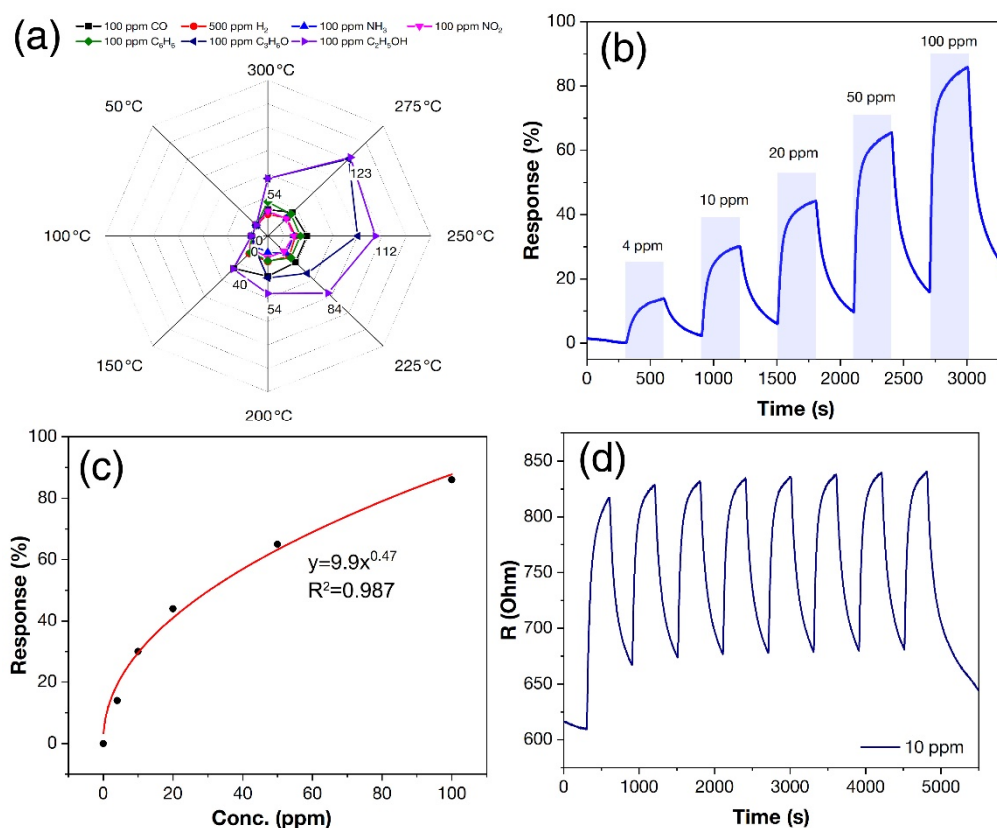
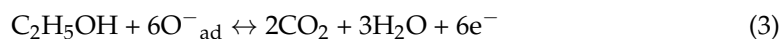


Figure 11. Selectivity diagram to different gases at an operating temperature of 50–300 °C (a), sensor response to 4–100 ppm ethanol at 225 °C (b), sensor response dependence on ethanol concentration at 225 °C (c), signal reproducibility when detecting 10 ppm ethanol at 225 °C (d).

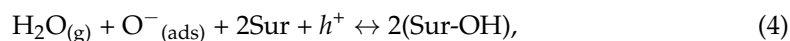
As the ethanol concentration increased from 4 to 100 ppm at an operating temperature of 225 °C, there was a consistent rise in electrical resistance relative to the baseline and the sensory response from 14 to 84% (Figure 11b). The increase in resistance during exposure to the reducing analyte is an indirect confirmation of the *p*-type conductivity of the receptor material under study (NiCo₂O₄). The established dependence of the sensory response on ethanol concentration (Figure 11c) is well described by the Freundlich isotherm equation: $S = kC^a$, where k and a are proportional and exponential constants representing adsorption capacity and adsorption intensification, respectively [74]. In our case, the equation has the form: $S = 9.9C^{0.47}$ (the determination coefficient (R^2) value is 0.987). This dependence is typical for chemoresistive gas sensors and agrees well with the available literature data [75,76]. Good reproducibility of the sensor response when detecting 10 ppm ethanol was demonstrated during 8 gas cycles (Figure 11d).

The ethanol detection mechanism using NiCo₂O₄ oxide with spinel structure as a receptor material can be described using the generally accepted notions of the analyte interactions with the *p*-type semiconductor surface [77,78]. Thus, in the ambient atmosphere at elevated temperatures, oxygen molecules adsorb on the semiconductor surface, which leads to a change in the material electrical resistance as electrons from the conduction band

reduce O_2 to the ionic form (reaction 2). In this case, O^{2-} , O^- or O_2^- ion-sorbed forms are possible depending on the operating temperature [79]. At the intermediate operating temperatures (including 225 °C), the O^- form is presumably formed, and the presence of such oxygen ions on the semiconductor surface promotes the generation of a core-shell type electronic structure. Here, the core is the inner volume of the semiconductor particle, and the shell is the hole accumulation layer, HAL [80], formed as a result of electron depletion for the O_2 to O^- reduction. In the presence of ethanol, a redox reaction occurs at the semiconductor surface between the O^- ions and the analyte, where the latter undergoes oxidation (reaction 3) [81]. The released electrons recombine with holes, leading to an increase in resistance, as observed in our case (Figure 11b). There are some publications in the literature [15,81–84] where $NiCo_2O_4$ is used as a sensing component of resistive gas sensors for VOC's at intermediate and elevated temperatures, which can be explained by its catalytic activity with respect to these analytes. In addition, the efficiency of the material in this case is largely determined by its microstructural characteristics, and a highly porous state with a hierarchical self-organization of the nanomaterial can contribute to an extra enhancement of its interaction activity with the surrounding atmosphere.



The effect of relative humidity (RH) on the sensory response when detecting 10 ppm ethanol was also studied during chemosensor measurements (Figure 12). Thus, as the RH rises from 0 to 80%, there is a consistent increase in baseline resistance (Figure 12a), as well as a decrease in the response value from 14 to 9% and from 44 to 35% upon detecting 4 and 20 ppm ethanol, respectively (Figure 12b). Nevertheless, the sensory response profile and signal-to-noise ratio remain unchanged over a wide range of relative humidity. In an atmosphere of elevated RH, hydroxyl groups can form on the surface of the $NiCo_2O_4$ film by the following mechanism [85,86]:



where Sur is the cobalt and nickel cations at the lattice sites on the surface of the $NiCo_2O_4$ film under study. As a result of this reaction, the main charge carriers (h^+) of $NiCo_2O_4$ are used, increasing the electrical resistance, as observed in our case (Figure 10a). The formed hydroxyl groups on the material surface occupy active centers that could be used for analyte gas sorption, resulting in a slight decrease in the sensory response (Figure 12a). The obtained results indicate that the alteration in atmospheric humidity does not lead to significant changes in the sensor response value and the kinetics of the surface processes during ethanol detecting. This feature of the material under study is extremely important from the practical point of view, since the sensing of gases under real conditions in the most cases occurs at elevated humidity.

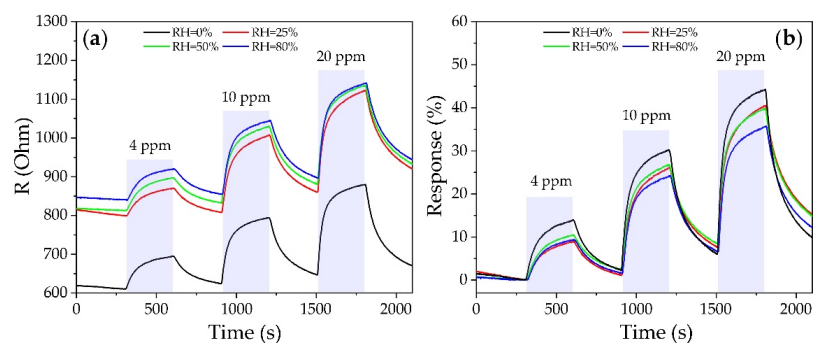


Figure 12. Sensor signal variations when detecting 4–20 ppm ethanol at 225 °C and different RH (0–80%): resistance (a) and sensor response (b).

4. Conclusions

With the combination of chemical coprecipitation and hydrothermal treatment of the obtained disperse system, NiCo₂O₄ nanopowder with several levels of microstructure self-organization was obtained—initial oxide nanoparticles of slightly elongated shape (average length is 11.2 ± 1.5 nm and average thickness is 5.4 ± 0.4 nm) are self-organized into nanosheets of about 10 nm thickness, which in turn are aggregated into hierarchically organized cellular agglomerates approximately 2 μ m in size. Since triethanolamine was employed as a precipitating agent, a hydrotalcite-like nickel-cobalt layered double hydroxide with an admixture of hexagonal metal hydroxocarbonate hydrate of $M(\text{CO}_3)_{0.5}\text{OH}\cdot 0.11\text{H}_2\text{O}$ composition (where M is nickel and cobalt cations) was obtained as a semiproduct. The additional heat treatment of the intermediate product at 400 °C (5 h) resulted in its complete decomposition and the formation of the NiCo₂O₄ oxide with the spinel structure (the average CSR size was 9.0 ± 1.0 nm). The powder formation of the aimed crystal structure was confirmed by XRD, SAED and HR-TEM. The target metal ratio was confirmed by EDX, and the uniform distribution of elements (Ni, Co and O) was proved by plotting the corresponding maps. The resulting nanopowder was used to prepare functional inks with sedimentation stability and rheological properties suitable for the microplotter printing of the NiCo₂O₄ film on the Pt/Al₂O₃/Pt chip surface. The morphology of the oxide film was found to be fully inherited from the hierarchically organized oxide nanopowder used, having two levels of particle self-organization. It was shown that the obtained film is highly porous and has a cellular microstructure, providing high sorption capacity and access of all initial NiCo₂O₄ nanoparticles to the external atmosphere, which is necessary to ensure high efficiency of the material as a receptor component of a resistive gas sensor. The AFM revealed the film thickness (15 μ m) and found the root mean square roughness (R_q) of the film over an area of 25 μm^2 to be 72 nm, while the maximum height difference in the studied representative area is 500 nm, which confirms the developed material surface. KPFM data indicated that the surface potential was shifted to deeper areas, suggesting that the charge carriers were shifted to these regions of the oxide films. The work function value of the material surface (4.54 eV) was significantly lower compared to those found in the literature, and may indicate the peculiarities of the obtained material related to the increased concentration of oxygen vacancies. Probably, in our case these electrophysical properties of the material were caused by the specifics of the synthesis process where triethanolamine was used as a reagent as well as the hydrothermal treatment stage of the solid phase particles formed by the programmed coprecipitation method. The electronic state of the elements in the film under study was studied using XPS. According to the results obtained, both metals are in the Me^{2+} and Me^{3+} forms. The oxygen O1s spectrum with regard to element concentrations can be divided into five peaks, two of which refer to oxygen-containing carbon derivatives, a peak with a position of 533.2 eV and FWHM 1.8 eV can be attributed to adsorbed H₂O vapor, and two peaks referring to the oxide material of the film. The conducted chemosensor measurements demonstrated that the printed NiCo₂O₄ film shows selectivity in the detection of ethanol at an operating temperature of 225 °C. The sensory response dependence for this analyte at concentrations of 4–100 ppm was determined. In addition, high signal reproducibility was shown when detecting 10 ppm ethanol. With an increase in relative humidity from 0 to 80%, a consistent baseline resistance growth is observed, as well as a decrease in the response value from 14 to 9% and from 44 to 35% upon detecting 4 and 20 ppm ethanol, respectively. Nevertheless, the sensory response profile and signal-to-noise ratio remain unchanged over a wide range of relative humidity. The efficiency of the material in this case is significantly affected by its microstructural characteristics, and the highly porous state of the hierarchical nanomaterial can provide an additional improvement of its interaction activity with the surrounding atmosphere.

Author Contributions: Conceptualization, T.L.S. and N.P.S.; investigation, T.L.S., A.S.M., P.Y.G., A.A.L., O.Y.G., N.P.S. and E.P.S.; writing—original draft preparation, T.L.S., P.Y.G., A.S.M., A.A.L. and O.Y.G.; writing—review and editing, N.P.S., E.P.S. and N.T.K.; visualization, T.L.S., A.S.M., P.Y.G.,

O.Y.G. and N.P.S.; supervision, N.P.S., E.P.S. and N.T.K.; funding acquisition, T.L.S. All authors have read and agreed to the published version of the manuscript.

Funding: This work was supported by the Council for Grants of the President of the Russian Federation for the state support of young Russian scientists (grant MK-1749.2022.1.3). XRD and SEM studies were carried out using shared experimental facilities supported by the Ministry of Science and Higher Education of the Russian Federation as part of the IGIC RAS state assignment.

Institutional Review Board Statement: Not applicable.

Informed Consent Statement: Not applicable.

Data Availability Statement: Not applicable.

Conflicts of Interest: The authors declare no conflict of interest.

References

1. Kumar, V.; Mariappan, C.R.; Azmi, R.; Moock, D.; Indris, S.; Bruns, M.; Ehrenberg, H.; Vijaya Prakash, G. Pseudocapacitance of Mesoporous Spinel-Type $M\text{Co}_2\text{O}_4$ ($M = \text{Co}, \text{Zn}, \text{and Ni}$) Rods Fabricated by a Facile Solvothermal Route. *ACS Omega* **2017**, *2*, 6003–6013. [[CrossRef](#)] [[PubMed](#)]
2. Guragain, D.; Zequine, C.; Gupta, R.K.; Mishra, S.R. Facile Synthesis of Bio-Template Tubular $M\text{Co}_2\text{O}_4$ ($M = \text{Cr}, \text{Mn}, \text{Ni}$) Microstructure and Its Electrochemical Performance in Aqueous Electrolyte. *Processes* **2020**, *8*, 343. [[CrossRef](#)]
3. Mohamed, S.G.; Tsai, Y.-Q.; Chen, C.-J.; Tsai, Y.-T.; Hung, T.-F.; Chang, W.-S.; Liu, R.-S. Ternary Spinel $M\text{Co}_2\text{O}_4$ ($M = \text{Mn}, \text{Fe}, \text{Ni}, \text{and Zn}$) Porous Nanorods as Bifunctional Cathode Materials for Lithium– O_2 Batteries. *ACS Appl. Mater. Interfaces* **2015**, *7*, 12038–12046. [[CrossRef](#)] [[PubMed](#)]
4. Chen, M.; Huang, X.; Chen, C.; Hou, W.; Xu, Y. M-Dependent activity of $M\text{Co}_2\text{O}_4$ spinels for water splitting and H_2 production on $\text{Zn}_{0.5}\text{Cd}_{0.5}\text{S}$ under visible light. *Appl. Catal. B Environ.* **2021**, *298*, 120469. [[CrossRef](#)]
5. Li, G.; Li, L.; Shi, J.; Yuan, Y.; Li, Y.; Zhao, W.; Shi, J. One-pot pyrolytic synthesis of mesoporous $M\text{Co}_2\text{O}_{4(4.5)}$ ($M = \text{Mn}, \text{Ni}, \text{Fe}, \text{Cu}$) spinels and its high efficient catalytic properties for CO oxidation at low temperature. *J. Mol. Catal. A Chem.* **2014**, *390*, 97–104. [[CrossRef](#)]
6. Macias, J.D.; Bacelis-Martinez, R.D.; Ruiz-Gomez, M.A.; Bante-Guerra, J.; Villafan-Vidales, H.I.; Rodriguez-Gattorno, G.; Romero-Paredes, H.; Alvarado-Gil, J.J. Thermophysical and optical properties of $\text{NiCo}_2\text{O}_4@\text{ZrO}_2$: A potential composite for thermochemical processes. *Int. J. Hydrogen Energy* **2021**, *46*, 10632–10641. [[CrossRef](#)]
7. Bagtache, R.; Boudjedien, K.; Sebai, I.; Meziani, D.; Trari, M. Facile preparation of the spinel CuCo_2O_4 Application to hydrogen photo-production. *Appl. Phys. A* **2021**, *127*, 60. [[CrossRef](#)]
8. Qu, F.; Jiang, H.; Yang, M. MOF-derived $\text{Co}_3\text{O}_4/\text{NiCo}_2\text{O}_4$ double-shelled nanocages with excellent gas sensing properties. *Mater. Lett.* **2017**, *190*, 75–78. [[CrossRef](#)]
9. Joshi, N.; da Silva, L.F.; Jadhav, H.; M'Peko, J.-C.; Millan Torres, B.B.; Aguir, K.; Mastelaro, V.R.; Oliveira, O.N. One-step approach for preparing ozone gas sensors based on hierarchical NiCo_2O_4 structures. *RSC Adv.* **2016**, *6*, 92655–92662. [[CrossRef](#)]
10. Kumar, R. NiCo_2O_4 Nano-/Microstructures as High-Performance Biosensors: A Review. *Nano-Micro Lett.* **2020**, *12*, 122. [[CrossRef](#)]
11. Gonçalves, J.M.; Rocha, D.P.; Silva, M.N.T.; Martins, P.R.; Nossol, E.; Angnes, L.; Rout, C.S.; Munoz, R.A.A. Feasible strategies to promote the sensing performances of spinel $M\text{Co}_2\text{O}_4$ ($M = \text{Ni}, \text{Fe}, \text{Mn}, \text{Cu}$ and Zn) based electrochemical sensors: A review. *J. Mater. Chem. C* **2021**, *9*, 7852–7887. [[CrossRef](#)]
12. Hu, Y.; Li, T.; Zhang, J.; Guo, J.; Wang, W.; Zhang, D. High-sensitive NO_2 sensor based on p- $\text{NiCo}_2\text{O}_4/n\text{-WO}_3$ heterojunctions. *Sens. Actuators B Chem.* **2022**, *352*, 130912. [[CrossRef](#)]
13. Basirun, W.J.; Saeed, I.M.; Rahman, M.S.; Mazari, S.A. Nickel oxides/hydroxides-graphene as hybrid supercapattery nanocomposites for advanced charge storage materials—A review. *Crit. Rev. Solid State Mater. Sci.* **2021**, *46*, 553–586. [[CrossRef](#)]
14. Kim, S.-H.; Yun, K.-S. Room-temperature hydrogen gas sensor composed of palladium thin film deposited on NiCo_2O_4 nanoneedle forest. *Sens. Actuators B Chem.* **2023**, *376*, 132958. [[CrossRef](#)]
15. Chen, Q.; Zhang, Y.; Ma, S.; Wang, Y.; Wang, P.; Zhang, G.; Gengzang, D.; Jiao, H.; Wang, M.; Chen, W. Multishelled $\text{NiO}/\text{NiCo}_2\text{O}_4$ hollow microspheres derived from bimetal-organic frameworks as high-performance sensing material for acetone detection. *J. Hazard. Mater.* **2021**, *415*, 125662. [[CrossRef](#)]
16. Wang, D.; Mi, Q.; Zhang, H.; Li, G.; Zhang, D. Sensitive Xylene Gas Sensor Based on $\text{NiO}-\text{NiCo}_2\text{O}_4$ Hierarchical Spherical Structure Constructed With Nanorods. *IEEE Sens. J.* **2022**, *22*, 10346–10352. [[CrossRef](#)]
17. Dang, F.; Wang, Y.; Gao, J.; Xu, L.; Cheng, P.; Lv, L.; Zhang, B.; Li, X.; Wang, C. Hierarchical flower-like NiCo_2O_4 applied in n-butanol detection at low temperature. *Sens. Actuators B Chem.* **2020**, *320*, 128577. [[CrossRef](#)]
18. Wang, Q.; Bai, J.; Huang, B.; Hu, Q.; Cheng, X.; Li, J.; Xie, E.; Wang, Y.; Pan, X. Design of $\text{NiCo}_2\text{O}_4@\text{SnO}_2$ heterostructure nanofiber and their low temperature ethanol sensing properties. *J. Alloys Compd.* **2019**, *791*, 1025–1032. [[CrossRef](#)]
19. Gai, L.-Y.; Lai, R.-P.; Dong, X.-H.; Wu, X.; Luan, Q.-T.; Wang, J.; Lin, H.-F.; Ding, W.-H.; Wu, G.-L.; Xie, W.-F. Recent advances in ethanol gas sensors based on metal oxide semiconductor heterojunctions. *Rare Met.* **2022**, *41*, 1818–1842. [[CrossRef](#)]

20. Yang, S.; Lei, G.; Xu, H.; Lan, Z.; Wang, Z.; Gu, H. Metal Oxide Based Heterojunctions for Gas Sensors: A Review. *Nanomaterials* **2021**, *11*, 1026. [[CrossRef](#)]
21. Rao, B.B. Zinc oxide ceramic semi-conductor gas sensor for ethanol vapour. *Mater. Chem. Phys.* **2000**, *64*, 62–65. [[CrossRef](#)]
22. Wang, L.; Kang, Y.; Liu, X.; Zhang, S.; Huang, W.; Wang, S. ZnO nanorod gas sensor for ethanol detection. *Sens. Actuators B Chem.* **2012**, *162*, 237–243. [[CrossRef](#)]
23. Zheng, J.; Zhang, T.; Zeng, H.; Guo, W.; Zhao, B.; Sun, Y.; Li, Y.; Jiang, L. Multishelled Hollow Structures of Yttrium Oxide for the Highly Selective and Ultrasensitive Detection of Methanol. *Small* **2019**, *15*, 1804688. [[CrossRef](#)] [[PubMed](#)]
24. Klym, H.; Ingram, A.; Shpotyuk, O.; Hadzaman, I.; Solntsev, V.; Hotra, O.; Popov, A.I. Positron annihilation characterization of free volume in micro- and macro-modified $\text{Cu}_{0.4}\text{Co}_{0.4}\text{Ni}_{0.4}\text{Mn}_{1.8}\text{O}_4$ ceramics. *Low Temp. Phys.* **2016**, *42*, 601–605. [[CrossRef](#)]
25. Joshi, R.K.; Schneider, J.J. Assembly of one dimensional inorganic nanostructures into functional 2D and 3D architectures. Synthesis, arrangement and functionality. *Chem. Soc. Rev.* **2012**, *41*, 5285. [[CrossRef](#)]
26. Yu, Z.; Tetard, L.; Zhai, L.; Thomas, J. Supercapacitor electrode materials: Nanostructures from 0 to 3 dimensions. *Energy Environ. Sci.* **2015**, *8*, 702–730. [[CrossRef](#)]
27. Pham, T.N.; Huy, T.Q.; Le, A.-T. Spinel ferrite (AFe_2O_4)-based heterostructured designs for lithium-ion battery, environmental monitoring, and biomedical applications. *RSC Adv.* **2020**, *10*, 31622–31661. [[CrossRef](#)]
28. Yan, M.; Jiang, F.; Liu, Y.; Sun, L.; Bai, H.; Zhu, F.; Shi, W. Flexible mixed metal oxide hollow spheres/RGO hybrid lamellar films for high performance supercapacitors. *Colloids Surf. A Physicochem. Eng. Asp.* **2021**, *612*, 125902. [[CrossRef](#)]
29. Jin, J.; Dai, Y.; Lu, J.; Dai, X.; Tie, N.; Ma, F.; Wang, W.; Pu, L.; Zhang, H. Hydrothermal synthesis of NiO/NiCo₂O₄ nanomaterials for applications in electrochemical energy storage. *J. Mater. Sci. Mater. Electron.* **2022**, *33*, 354–366. [[CrossRef](#)]
30. Liu, S.; Liu, L.; Wang, W.; Zhou, Y.; Dai, G.; Liu, Y. Enhanced Non-Enzymatic Glucose Detection Using a Flower-Like NiCo₂O₄ Spheres Modified Electrode. *J. Anal. Chem.* **2021**, *76*, 993–1001. [[CrossRef](#)]
31. Ji, J.; Xu, J.; Fan, G.; Guo, T.; Yang, L.; Li, F. Controlled synthesis of CeO_x-NiCo₂O₄ nanocomposite with 3D umbrella-shaped hierarchical structure: A sharp-tip enhanced electrocatalyst for efficient oxygen evolution reaction over a broad pH region. *Electrochim. Acta* **2021**, *382*, 138345. [[CrossRef](#)]
32. Wang, Q.; Liu, X.; Ju, T.; Ying, Z.; Xie, J.; Zhang, Y. Preparation and electrochemical properties of NiCo₂O₄ nanorods grown on nickel foam filled by carbon-coated attapulgite for supercapacitors. *Mater. Res. Express* **2019**, *6*, 125524. [[CrossRef](#)]
33. Hui, Z.; Yao, S.; Ou, T.K.; Liu, Q.; Zhi, L.; Cao, Y.; Sun, Y. Soft-template-assisted Synthesis of Hierarchical NiCo₂O₄ array/Ni foam for application in supercapacitors. *Int. J. Electrochem. Sci.* **2022**, *17*, 220422. [[CrossRef](#)]
34. John, G.; Gopalakrishnan, S.; Sharan, A.; Navaneethan, M.; Kulandaivel, J.; Singh, N.; Justin Jesuraj, P. Exploring the Heterostructure Engineering of SnS/NiCo₂O₄ for Overall Water Splitting. *Energy Fuels* **2022**, *37*, 624–634. [[CrossRef](#)]
35. Arbaz, S.J.; Sekhar, S.C.; Ramulu, B.; Yu, J.S. Binder-free preparation of bimetallic oxide vertical nanosheet arrays toward high-rate performance and energy density supercapacitors. *Int. J. Energy Res.* **2021**, *45*, 13999–14009. [[CrossRef](#)]
36. Zhou, J.; Yang, X.; Zhang, Y.; Jia, J.; He, X.; Yu, L.; Pan, Y.; Liao, J.; Sun, M.; He, J. Interconnected NiCo₂O₄ nanosheet arrays grown on carbon cloth as a host, adsorber and catalyst for sulfur species enabling high-performance Li-S batteries. *Nanoscale Adv.* **2021**, *3*, 1690–1698. [[CrossRef](#)]
37. Hunge, Y.M.; Yadav, A.A.; Kang, S.W.; Kim, H.; Fujishima, A.; Terashima, C. Nanoflakes-like nickel cobaltite as active electrode material for 4-nitrophenol reduction and supercapacitor applications. *J. Hazard. Mater.* **2021**, *419*, 126453. [[CrossRef](#)]
38. Gopalakrishnan, A.; Badhulika, S. Hierarchical Architected Dahlia Flower-Like NiCo₂O₄/NiCoSe₂ as a Bifunctional Electrode for High-Energy Supercapacitor and Methanol Fuel Cell Application. *Energy Fuels* **2021**, *35*, 9646–9659. [[CrossRef](#)]
39. Isacfranklin, M.; Ravi, G.; Yuvakkumar, R.; Kumar, P.; Velauthapillai, D.; Saravanakumar, B.; Thambidurai, M.; Dang, C. Urchin like NiCo₂O₄/rGO nanocomposite for high energy asymmetric storage applications. *Ceram. Int.* **2020**, *46*, 16291–16297. [[CrossRef](#)]
40. Yan, S.; Luo, S.; Sun, M.; Wang, Q.; Zhang, Y.; Liu, X. Facile hydrothermal synthesis of urchin-like NiCo₂O₄ as advanced electrochemical pseudocapacitor materials. *Int. J. Energy Res.* **2021**, *45*, 20186–20198. [[CrossRef](#)]
41. Sundriyal, P.; Bhattacharya, S. Scalable Micro-fabrication of Flexible, Solid-State, Inexpensive, and High-Performance Planar Micro-supercapacitors through Inkjet Printing. *ACS Appl. Energy Mater.* **2019**, *2*, 1876–1890. [[CrossRef](#)]
42. Ge, L.; Ye, X.; Yu, Z.; Chen, B.; Liu, C.; Guo, H.; Zhang, S.; Sassa, F.; Hayashi, K. A fully inkjet-printed disposable gas sensor matrix with molecularly imprinted gas-selective materials. *NPJ Flex. Electron.* **2022**, *6*, 40. [[CrossRef](#)]
43. Bacelis-Martínez, R.D.; Oskam, G.; Rodríguez Gattorno, G.; Ruiz-Gómez, M.A. Inkjet Printing as High-Throughput Technique for the Fabrication of NiCo₂O₄ Films. *Adv. Mater. Sci. Eng.* **2017**, *2017*. [[CrossRef](#)]
44. Li, Z.; Yu, J.; Dong, D.; Yao, G.; Wei, G.; He, A.; Wu, H.; Zhu, H.; Huang, Z.; Tang, Z. E-nose based on a high-integrated and low-power metal oxide gas sensor array. *Sens. Actuators B Chem.* **2023**, *380*, 133289. [[CrossRef](#)]
45. Kravchenko, D.E.; Matavž, A.; Rubio-Giménez, V.; Vanduffel, H.; Verstreken, M.; Ameloot, R. Aerosol Jet Printing of the Ultramicroporous Calcium Squarate Metal-Organic Framework. *Chem. Mater.* **2022**, *34*, 6809–6814. [[CrossRef](#)]
46. Verma, A.; Goos, R.; Weerd, J.D.; Pelgrims, P.; Ferraris, E. Design, Fabrication, and Testing of a Fully 3D-Printed Pressure Sensor Using a Hybrid Printing Approach. *Sensors* **2022**, *22*, 7531. [[CrossRef](#)]
47. Fisher, C.; Warmack, B.J.; Yu, Y.; Skolrood, L.N.; Li, K.; Joshi, P.C.; Saito, T.; Aytug, T. All-aerosol-jet-printed highly sensitive and selective polyaniline-based ammonia sensors: A route toward low-cost, low-power gas detection. *J. Mater. Sci.* **2021**, *56*, 12596–12606. [[CrossRef](#)]

48. Simonenko, T.L.; Simonenko, N.P.; Gorobtsov, P.Y.; Pozharnitskaya, V.M.; Simonenko, E.P.; Glumov, O.V.; Melnikova, N.A.; Sevastyanov, V.G.; Kuznetsov, N.T. Pen Plotter Printing of MnO_x Thin Films Using Manganese Alkoxoacetylacetonate. *Russ. J. Inorg. Chem.* **2021**, *66*, 1416–1424. [[CrossRef](#)]
49. Simonenko, T.L.; Simonenko, N.P.; Gorobtsov, P.Y.; Mokrushin, A.S.; Solovey, V.R.; Pozharnitskaya, V.M.; Simonenko, E.P.; Glumov, O.V.; Melnikova, N.A.; Lizunova, A.A.; et al. Pen plotter printing of Co_3O_4 thin films: Features of the microstructure, optical, electrophysical and gas-sensing properties. *J. Alloys Compd.* **2020**, *832*, 154957. [[CrossRef](#)]
50. Liu, S.; Cao, R.; Wu, J.; Guan, L.; Li, M.; Liu, J.; Tian, J. Directly writing barrier-free patterned biosensors and bioassays on paper for low-cost diagnostics. *Sens. Actuators B Chem.* **2019**, *285*, 529–535. [[CrossRef](#)]
51. Simonenko, T.L.; Simonenko, N.P.; Gorobtsov, P.Y.; Vlasov, I.S.; Solovey, V.R.; Shelaev, A.V.; Simonenko, E.P.; Glumov, O.V.; Melnikova, N.A.; Kozodaev, M.G.; et al. Microplotter printing of planar solid electrolytes in the $\text{CeO}_2\text{--Y}_2\text{O}_3$ system. *J. Colloid Interface Sci.* **2021**, *588*, 209–220. [[CrossRef](#)] [[PubMed](#)]
52. Simonenko, T.L.; Simonenko, N.P.; Simonenko, E.P.; Vlasov, I.S.; Volkov, I.A.; Kuznetsov, N.T. Microplotter Printing of Hierarchically Organized Planar NiCo_2O_4 Nanostructures. *Russ. J. Inorg. Chem.* **2022**, *67*, 1848–1854. [[CrossRef](#)]
53. Fedorov, F.S.; Simonenko, N.P.; Trouillet, V.; Volkov, I.A.; Plugin, I.A.; Rupasov, D.P.; Mokrushin, A.S.; Nagornov, I.A.; Simonenko, T.L.; Vlasov, I.S.; et al. Microplotter-Printed On-Chip Combinatorial Library of Ink-Derived Multiple Metal Oxides as an “Electronic Olfaction” Unit. *ACS Appl. Mater. Interfaces* **2020**, *12*, 56135–56150. [[CrossRef](#)]
54. Simonenko, T.L.; Simonenko, N.P.; Gorobtsov, P.Y.; Simonenko, E.P.; Kuznetsov, N.T. Microextrusion Printing of Multilayer Hierarchically Organized Planar Nanostructures Based on NiO , $(\text{CeO}_2)_{0.8}(\text{Sm}_2\text{O}_3)_{0.2}$ and $\text{La}_{0.6}\text{Sr}_{0.4}\text{Co}_{0.2}\text{Fe}_{0.8}\text{O}_{3-\delta}$. *Micromachines* **2022**, *14*, 3. [[CrossRef](#)] [[PubMed](#)]
55. Simonenko, T.L.; Simonenko, N.P.; Gorobtsov, P.Y.; Grafov, O.Y.; Simonenko, E.P.; Kuznetsov, N.T. Synthesis of $((\text{CeO}_2)_{0.8}(\text{Sm}_2\text{O}_3)_{0.2})@\text{NiO}$ Core-Shell Type Nanostructures and Microextrusion Printing of a Composite Anode Based on Them. *Materials* **2022**, *15*, 8918. [[CrossRef](#)]
56. Gorobtsov, P.Y.; Mokrushin, A.S.; Simonenko, T.L.; Simonenko, N.P.; Simonenko, E.P.; Kuznetsov, N.T. Microextrusion Printing of Hierarchically Structured Thick V_2O_5 Film with Independent from Humidity Sensing Response to Benzene. *Materials* **2022**, *15*, 7837. [[CrossRef](#)]
57. Fisenko, N.A.; Solomatov, I.A.; Simonenko, N.P.; Mokrushin, A.S.; Gorobtsov, P.Y.; Simonenko, T.L.; Volkov, I.A.; Simonenko, E.P.; Kuznetsov, N.T. Atmospheric Pressure Solvothermal Synthesis of Nanoscale SnO_2 and Its Application in Microextrusion Printing of a Thick-Film Chemosensor Material for Effective Ethanol Detection. *Sensors* **2022**, *22*, 9800. [[CrossRef](#)]
58. Simonenko, N.P.; Kadyrov, N.S.; Simonenko, T.L.; Simonenko, E.P.; Sevastyanov, V.G.; Kuznetsov, N.T. Preparation of ZnS Nanopowders and Their Use in the Additive Production of Thick-Film Structures. *Russ. J. Inorg. Chem.* **2021**, *66*, 1283–1288. [[CrossRef](#)]
59. Porta, P.; Dragone, R.; Fierro, G.; Inversi, M.; Jacono, M.L.; Moretti, G. Preparation and characterisation of cobalt–copper hydroxysalts and their oxide products of decomposition. *J. Chem. Soc. Faraday Trans.* **1992**, *88*, 311–319. [[CrossRef](#)]
60. Yang, S.; Zhang, Z.; Zhou, J.; Sui, Z.; Zhou, X. Hierarchical NiCo LDH-rGO/Ni Foam Composite as Electrode Material for High-Performance Supercapacitors. *Trans. Tianjin Univ.* **2019**, *25*, 266–275. [[CrossRef](#)]
61. Wang, J.; Gao, F.; Du, X.; Ma, X.; Hao, X.; Ma, W.; Wang, K.; Guan, G.; Abudula, A. A high-performance electroactive PPy/rGO/NiCo-LDH hybrid film for removal of dilute dodecyl sulfonate ions. *Electrochim. Acta* **2020**, *331*, 135288. [[CrossRef](#)]
62. Simonenko, T.L.; Simonenko, N.P.; Gorobtsov, P.Y.; Klyuev, A.L.; Grafov, O.Y.; Ivanova, T.M.; Simonenko, E.P.; Sevastyanov, V.G.; Kuznetsov, N.T. Hydrothermally synthesized hierarchical $\text{Ce}_{1-x}\text{Sm}_x\text{O}_{2-\delta}$ oxides for additive manufacturing of planar solid electrolytes. *Ceram. Int.* **2022**, *48*, 22401–22410. [[CrossRef](#)]
63. Valdez, R.; Grotjahn, D.B.; Smith, D.K.; Quintana, J.M.; Olivias, A. Nanosheets of Co-(Ni and Fe) layered double hydroxides for electrocatalytic water oxidation reaction. *Int. J. Electrochem. Sci.* **2015**, *10*, 909–918.
64. Marimuthu, G.; Palanisamy, G.; Pazhanivel, T.; Bharathi, G.; Christopher, M.M.; Jeyadheepan, K. Nanorod like NiCo_2O_4 nanostructure for high sensitive and selective ammonia gas sensor. *J. Mater. Sci. Mater. Electron.* **2020**, *31*, 1951–1959. [[CrossRef](#)]
65. Cai, Y.; Ma, J.; Wang, T. Hydrothermal synthesis of $\alpha\text{-Ni}(\text{OH})_2$ and its conversion to NiO with electrochemical properties. *J. Alloys Compd.* **2014**, *582*, 328–333. [[CrossRef](#)]
66. Yang, J.; Cheng, H.; Frost, R.L. Synthesis and characterisation of cobalt hydroxy carbonate $\text{Co}_2\text{CO}_3(\text{OH})_2$ nanomaterials. *Spectrochim. Acta Part A Mol. Biomol. Spectrosc.* **2011**, *78*, 420–428. [[CrossRef](#)]
67. Zakutayev, A.; Paudel, T.R.; Ndione, P.F.; Perkins, J.D.; Lany, S.; Zunger, A.; Ginley, D.S. Cation off-stoichiometry leads to high p-type conductivity and enhanced transparency in Co_2ZnO_4 thin films. *Phys. Rev. B* **2012**, *85*, 085204. [[CrossRef](#)]
68. Chen, W.; Wei, L.; Lin, Z.; Liu, Q.; Chen, Y.; Lin, Y.; Huang, Z. Hierarchical flower-like $\text{NiCo}_2\text{O}_4@\text{TiO}_2$ hetero-nanosheets as anodes for lithium ion batteries. *RSC Adv.* **2017**, *7*, 47602–47613. [[CrossRef](#)]
69. Pathak, M.; Mutadak, P.; Mane, P.; More, M.A.; Chakraborty, B.; Late, D.J.; Rout, C.S. Enrichment of the field emission properties of NiCo_2O_4 nanostructures by UV/ozone treatment. *Mater. Adv.* **2021**, *2*, 2658–2666. [[CrossRef](#)]
70. Simonenko, T.L.; Simonenko, N.P.; Gorobtsov, P.Y.; Dudorova, D.A.; Simonenko, E.P.; Sevastyanov, V.G.; Kuznetsov, N.T. Triethanolamine-Assisted Hydrothermal Synthesis of Hierarchically Organized Nickel Oxide Particles. *Russ. J. Inorg. Chem.* **2022**, *67*, 622–627. [[CrossRef](#)]
71. Wang, W.; Li, Z.; Meng, A.; Li, Q. Network-like holey NiCo_2O_4 nanosheet arrays on Ni foam synthesized by electrodeposition for high-performance supercapacitors. *J. Solid State Electrochem.* **2019**, *23*, 635–644. [[CrossRef](#)]

72. Shirley, D.A. High-Resolution X-Ray Photoemission Spectrum of the Valence Bands of Gold. *Phys. Rev. B* **1972**, *5*, 4709–4714. [[CrossRef](#)]
73. Biesinger, M.C.; Payne, B.P.; Grosvenor, A.P.; Lau, L.W.M.; Gerson, A.R.; Smart, R.S.C. Resolving surface chemical states in XPS analysis of first row transition metals, oxides and hydroxides: Cr, Mn, Fe, Co and Ni. *Appl. Surf. Sci.* **2011**, *257*, 2717–2730. [[CrossRef](#)]
74. Mokrushin, A.S.; Nagornov, I.A.; Simonenko, T.L.; Simonenko, N.P.; Gorobtsov, P.Y.; Khamova, T.V.; Kopitsa, G.P.; Evzrezov, A.N.; Simonenko, E.P.; Sevastyanov, V.G.; et al. Chemoresistive gas-sensitive ZnO/Pt nanocomposites films applied by microplotter printing with increased sensitivity to benzene and hydrogen. *Mater. Sci. Eng. B* **2021**, *271*, 115233. [[CrossRef](#)]
75. Ambardekar, V.; Bandyopadhyay, P.P.; Majumder, S.B. Understanding on the ethanol sensing mechanism of atmospheric plasma sprayed 25 wt.%WO₃–75 wt.%SnO₂ coating. *Sens. Actuators B Chem.* **2019**, *290*, 414–425. [[CrossRef](#)]
76. McConnell, C.; Kanakaraj, S.N.; Dugre, J.; Malik, R.; Zhang, G.; Haase, M.R.; Hsieh, Y.Y.; Fang, Y.; Mast, D.; Shanov, V. Hydrogen Sensors Based on Flexible Carbon Nanotube-Palladium Composite Sheets Integrated with Ripstop Fabric. *ACS Omega* **2020**, *5*, 487–497. [[CrossRef](#)]
77. Ji, H.; Zeng, W.; Li, Y. Gas sensing mechanisms of metal oxide semiconductors: A focus review. *Nanoscale* **2019**, *11*, 22664–22684. [[CrossRef](#)]
78. Degler, D.; Weimar, U.; Barsan, N. Current Understanding of the Fundamental Mechanisms of Doped and Loaded Semiconducting Metal-Oxide-Based Gas Sensing Materials. *ACS Sens.* **2019**, *4*, 2228–2249. [[CrossRef](#)]
79. Kim, H.J.; Lee, J.H. Highly sensitive and selective gas sensors using p-type oxide semiconductors: Overview. *Sens. Actuators B Chem.* **2014**, *192*, 607–627. [[CrossRef](#)]
80. Jeong, S.Y.; Kim, J.S.; Lee, J.H. Rational Design of Semiconductor-Based Chemiresistors and their Libraries for Next-Generation Artificial Olfaction. *Adv. Mater.* **2020**, *32*, 2002075. [[CrossRef](#)]
81. Akhtar, A.; Sadaf, S.; Liu, J.; Wang, Y.; Wei, H.; Zhang, Q.; Fu, C.; Wang, J. Hydrothermally synthesized spherical g-C₃N₄-NiCo₂O₄ nanocomposites for ppb level ethanol detection. *J. Alloys Compd.* **2022**, *911*, 165048. [[CrossRef](#)]
82. Zhao, Y.; Yuan, X.; Sun, Y.; Wang, Q.; Xia, X.Y.; Tang, B. Facile synthesis of tortoise shell-like porous NiCo₂O₄ nanoplate with promising triethylamine gas sensing properties. *Sens. Actuators B Chem.* **2020**, *323*, 128663. [[CrossRef](#)]
83. Zheng, Y.; Wang, L.; Tian, H.; Qiao, L.; Zeng, Y.; Liu, C. Bimetal carbonaceous templates for multi-shelled NiCo₂O₄ hollow sphere with enhanced xylene detection. *Sens. Actuators B Chem.* **2021**, *339*, 129862. [[CrossRef](#)]
84. Akhtar, A.; Di, W.; Liu, J.; Fu, C.; Wang, J.; Chu, X. The detection of ethanol vapors based on a p-type gas sensor fabricated from heterojunction MoS₂-NiCo₂O₄. *Mater. Chem. Phys.* **2022**, *282*, 125964. [[CrossRef](#)]
85. Wicker, S.; Großmann, K.; Barsan, N.; Weimar, U. Co₃O₄—A systematic investigation of catalytic and gas sensing performance under variation of temperature, humidity, test gas and test gas concentration. *Sens. Actuators B Chem.* **2013**, *185*, 644–650. [[CrossRef](#)]
86. Mokoena, T.P.; Tshabalala, Z.P.; Hillie, K.T.; Swart, H.C.; Motaung, D.E. The blue luminescence of p-type NiO nanostructured material induced by defects: H₂S gas sensing characteristics at a relatively low operating temperature. *Appl. Surf. Sci.* **2020**, *525*, 146002. [[CrossRef](#)]

Disclaimer/Publisher's Note: The statements, opinions and data contained in all publications are solely those of the individual author(s) and contributor(s) and not of MDPI and/or the editor(s). MDPI and/or the editor(s) disclaim responsibility for any injury to people or property resulting from any ideas, methods, instructions or products referred to in the content.